Collective ERK/Akt activity waves orchestrate epithelial homeostasis by driving apoptosis-induced survival

Short title: **Collective ERK/Akt dynamics in epithelia**

Paolo Armando Gagliardi [1], Maciej Dobrzyński [1], Marc-Antoine Jacques [1], Coralie Dessauges [1], Robert M Hughes[2] and Olivier Pertz [1]*

[1] Institute of Cell Biology, University of Bern, Baltzerstrasse 4, 3012 Bern, Switzerland

[2] Department of Chemistry, East Carolina University, Greenville, North Carolina, USA

*Correspondence and requests for materials should be addressed to O.P. (email: olivier.pertz@izb.unibe.ch).

Abstract

Cell death events continuously challenge epithelial barrier function, yet are crucial to eliminate old or critically damaged cells. How such apoptotic events are spatio-temporally organized to maintain epithelial homeostasis remains unclear. We observe waves of Extracellular Signal-Regulated Kinase (ERK) and AKT serine/threonine kinase (Akt) activity pulses that originate from apoptotic cells and propagate radially to healthy surrounding cells. Such a propagation requires Epidermal Growth Factor Receptor (EGFR) and matrix metalloproteinase (MMP) signaling. At the single-cell level, ERK/Akt waves act as spatial survival signals that locally protect cells in the vicinity of the epithelial injury from apoptosis for a period of 3-4 hours. At the cell population level, ERK/Akt waves maintain epithelial homeostasis (EH) in response to mild or intense insults. Disruption of this spatial signaling system results in the inability of a model epithelial tissue to ensure barrier function in response to cellular stress.

Introduction

An epithelium is a self-organizing tissue that coordinates cell division and death to maintain its barrier function. This ability, called epithelial homeostasis (EH), is especially important due to frequent apoptosis observed in multiple epithelia, which can lead to complete tissue turnover in a few days in the intestinal epithelium (Darwich et al. 2014). EH takes advantage of behaviors, such as sensing of cell density, epithelial extrusion, spindle orientation, apoptotic-neighbor communication, and cell-cell adhesion dynamics to maintain barrier function and epithelial integrity (Macara et al. 2014). Coordination between epithelial extrusion and cell division is crucial to maintain an adequate cell density (Marinari et al. 2012; Gudipaty et al. 2017; Eisenhoffer et al. 2012). Coordination of apoptotic cells with healthy neighboring cells contributes to epithelial integrity by closing the gaps resulting from the extrusion of dying cells (Gagliardi et al. 2018; Gu et al. 2011). Apoptosis can control the fate of neighboring cells. Mitogenic factors produced by apoptotic cells induce proliferation in neighboring cells, enabling wound repair (Li et al. 2010). Apoptotic cells can however also induce further apoptosis in neighboring cells during developmental processes that require collective apoptosis (Pérez-Garijo et al. 2013). Apoptosis can trigger survival fates in surrounding healthy cells in the *Drosophila* wing imaginal disk (Bilak et al. 2014). These different processes imply coordination of signaling pathways that regulate proliferation, survival or apoptosis fates. However, how these signaling pathways are regulated at the single-cell level, and spatio-temporally integrated at the population level remains poorly understood.

Mitogen-activated protein kinase (MAPK)/ERK- Phosphoinositide-3 kinase (PI3K)/Akt signaling networks are crucial for regulation of cell fate. Beyond the classic work in which these pathways have been studied using population-averaged measurements, recent evidence has shown that ERK/Akt signaling dynamics fine-tune fate decisions at the single cell level. In epithelial cells, discrete ERK activity pulses of fixed amplitude and duration are observed at the single cell level (Albeck et al. 2013). The ERK pulse frequency depends on the epidermal growth factor (EGF) concentration the cells experience, which further correlates with the efficiency of cell-cycle entry. Together, this provides a relationship between the EGF dose and the proliferation fate. These ERK pulses emerge from the three-tiered Raf/MEK/ERK network structure with negative feedback from ERK to Raf (Santos et al. 2007; Ryu et al. 2016; Albeck et al. 2013), that provide ultrasensitivity and adaptation properties to shape their pulsatile dynamics. In addition to ERK pulses, Akt pulses that are synchronous with the latter have been observed in epithelial cells (Sampattavanich et al. 2018). These Akt pulses are thought to maintain metabolic stability in epithelia (Hung et al. 2017). Beyond the relationship that links EGF dose and proliferation fate, little is known about how ERK/Akt regulates additional single-cell fate decisions such as survival or apoptosis, and how the latter are integrated at the cell population level to ensure EH. Here, we show that in response to cellular insults, apoptosis triggers a wave of ERK/Akt activity pulses that radially propagates for about three healthy cell layers around apoptotic, extruding cells. This signaling wave requires EGFR and MMP-dependent signaling, and acts as a spatial survival signal that

locally protects cells from apoptosis for a period of 3-4 hours. This single cell behavior allows maintenance of population-level EH and tissue integrity in response to mild or intense cellular insults.

Results

Collective ERK/Akt activity waves propagate from apoptotic cells in quiescent unstimulated epithelium

To investigate single-cell ERK/Akt activity dynamics in epithelia, we stably transduced MCF10A cells with Histone 2B (H2B), ERK-KTR (Regot et al. 2014) and 1-396 Forkhead box O3 (FoxO3a) tagged with miRFP703 (Shcherbakova et al. 2016), mTurquoise2 (Goedhart et al. 2012) and mNeonGreen (Shaner et al. 2013), respectively (Fig. S1A). ERK-KTR and FoxO3a biosensors respectively report single-cell ERK and Akt activity by displaying reversible nuclear-to-cytosol translocation upon phosphorylation (Fig. S1B, Video S1). While FoxO3a can be sensitive to ERK-dependent inputs, this has been shown to be negligible in MCF10A cells (Sampattavanich et al. 2018). We then developed an automated image analysis pipeline to segment and track nuclei using the H2B-miRFP703 channel. This step is followed by the extraction of cytosolic to nuclear fluorescence intensities that quantifies ERK/Akt activities (Fig. S1C). As previously shown (Albeck et al. 2013; Sampattavanich et al. 2018), we observed that starved MCF10A cells show synchronous ERK and Akt activity pulses whose frequency increases with EGF stimulation (Fig.1A). The amplitudes of both ERK/Akt pulses were similar in presence or absence of EGF (Fig.S1D). Strikingly, visual examination (Fig. 1B, Video S2), as well as spatial clustering of signaling trajectories based on their time-averaged positions (Fig. 1C), revealed that starved monolayers frequently display spatially and temporally coordinated ERK/Akt activity pulses, resulting in collective signaling events.

We observed that such collective events are triggered by apoptosis, that results from stress due to EGF starvation, and consist of a wave of ERK/Akt activity pulses that originates from an apoptotic cell and radially propagates in healthy neighboring cells (Fig. 1D, Video S3). Classification of neighboring cells based on their topological relationship with the apoptotic cell revealed sequential triggering of a synchronous ERK/Akt activity pulse within each successive cell layer (Fig. 1E, F). In the first layer, ERK/Akt activity increases synchronously with apoptotic nuclear shrinkage and peaks at 10-15 minutes after this event (Fig. 1G, S1E). In the second/third cell layers, delayed ERK/Akt activity peaks at 15-20, and 20-30 minutes, respectively. An apoptotic cell can trigger a collective ERK/AKT activation that involves about 10 neighboring cells on average (Fig. 1H). The proportion of neighboring cells with ERK/Akt pulses sharply decreases across the layers; approximately 90% of cells are activated in the first, 30% in the second, and 10% in the third layer (Fig. 1I). Further, although pulse amplitude is constant in the first and second layer, we detected a small but significant reduction of ERK activity amplitude in the third layer (Fig. 1J). These results show that apoptotic cells induce radially propagating ERK/Akt signaling waves in neighboring healthy cells.

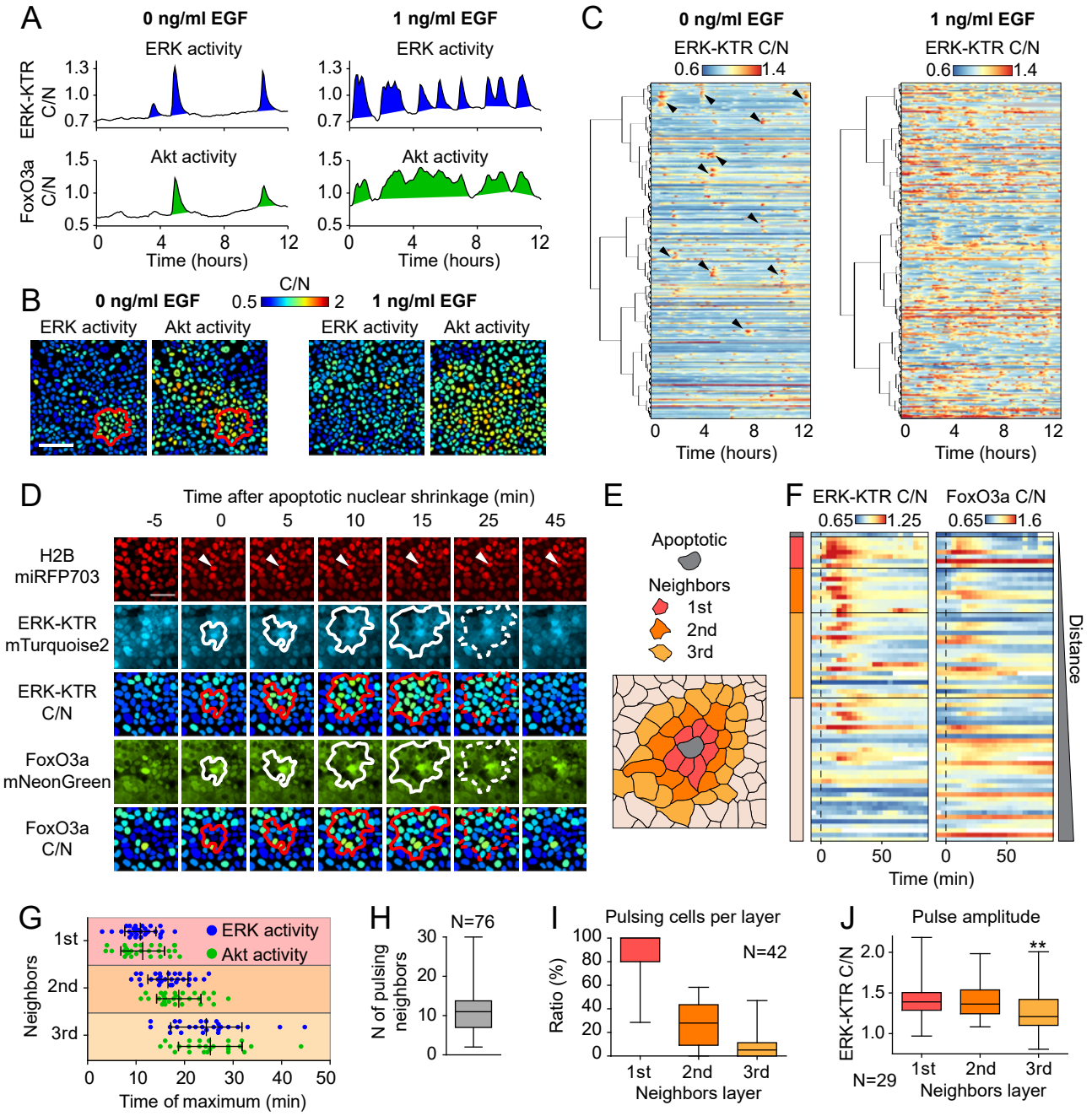

Figure 1: ERK/Akt waves propagate from apoptotic cells in starved MCF10A monolayers. (A) ERK/Akt activity trajectories measured by ERK-KTR-mTurquoise2 and FoxO3a-mNeonGreen biosensors in starved (left) and EGF-treated (right) MCF10A monolayers. Signaling trajectories of cytosolic/nuclear (C/N) fluorescence ratio of the respective biosensors are shown. **(B)** Micrographs of ERK/Akt activity in MCF10A monolayers. Single nuclei are color-coded for ERK/Akt C/N ratios. The red outline delimits a monolayer area showing spatially and temporally coordinated ERK/Akt pulses, hereinafter referred to as a collective event. **(C)** Spatial clustering of ERK trajectories. Heatmaps of color-coded ERK activity trajectories clustered according to their relative time-averaged position, i.e. adjacent trajectories in the heatmap represent cells in the same vicinity. Arrowheads indicate collective ERK activity events. **(D)** Timelapse micrographs of one collective ERK/Akt wave originating from an apoptotic cell. Nuclear marker, raw ERK-KTR, C/N ERK-KTR signal, raw FoxO3a, and C/N FoxO3a signal images are shown. Solid outlines denote the signaling wave propagation front. Dotted outlines denote cessation of the signaling wave. Warm/cold color-coded C/N signals indicate high/low signaling activity. **(E)** Topology of cell outlines of the event shown in D. **(F)** Spatially-clustered single-cell ERK/Akt trajectories from the collective event shown in D. Trajectories are ordered according to the time-averaged distance from the apoptotic cell. Rectangles on the left side indicate neighborhood layers shown in E. **(G)** Time of the maximum ERK/Akt activity according to the distribution of neighbors in relation to the apoptotic cell. Central line depicts the mean. Error bars represent the standard deviation. **(H)** Distribution of the number of pulsing neighbors around different apoptotic events. **(I)** Proportion of activated neighbors in the different neighborhood layers. **(J)** C/N ratio of maximal ERK-KTR amplitudes in activated cells in the different neighborhood layers. Box plots depict the median and the 25th and 75th percentiles; whiskers correspond to maximum and minimum values. T-test between 1st and 3rd layer (**, $P < 0.01$). Scale bars: (A) 100 µm, (D) 50 µm.

ERK/Akt waves are initiated during the early morphological events of apoptosis and are triggered independently from caspase activity

Execution of apoptosis is associated with a prototypical sequence of morphological events that include nuclear shrinkage, plasma membrane blebbing, chromatin condensation, extrusion of the apoptotic cell, nuclear fragmentation and disaggregation into apoptotic bodies (Saraste and Pulkki 2000). In epithelial cells, the two latter events are usually preceded by extrusion that removes the apoptotic body before fragmentation (Rosenblatt et al. 2001; Gagliardi et al. 2018). In MCF10A cells, extrusion however was only successful in 40% of apoptotic events, while in 60% of the events, formation of apoptotic bodies was occurring within the monolayer. The onset of the ERK/Akt waves coincided with nuclear shrinkage, the first event of the apoptosis sequence, which was then used as a reference to align the collective events (Fig. 2A, G). The other morphological hallmarks of apoptosis, including epithelial extrusion, occurred after the emergence of the collective signaling wave, ruling them out as potential initiators of the wave (Fig. 2B-G).

To causally link apoptosis with the initiation of a signaling wave, we used OptoBAX, an optogenetic apoptosis actuator, to selectively induce cell death with single-cell resolution (Godwin et al. 2019). Low efficiency transfection was used to achieve stochastic expression of plasmids encoding Cry2-BAX and a mitochondrion-anchored Cib fusion in the monolayer (Fig. 2H). Upon exposure to blue light, Cry2-BAX translocates to the mitochondrion and induces mitochondrial outer membrane permeabilization (MOMP) (Fig. 2I), causing apoptosis in less than an hour. Due to the biosensor and actuator's spectral requirements, we could only image one biosensor at a time, and focused on ERK-KTR. We observed that OptoBAX-induced apoptosis triggered an ERK wave identical to the one caused by spontaneous apoptosis (Fig. 2J).

To further delineate the mechanisms that trigger the signaling wave, we treated cells with zVAD-FMK, a pan-caspase inhibitor. ZVAD-FMK did not prevent ERK/Akt waves in neither spontaneous nor OptoBAX-triggered apoptosis (Fig. 2K, L, S2A-F, Video S5). Further, upon zVAD-FMK treatment, apoptotic signaling wave-triggering cells still displayed caspase-independent nuclear shrinkage and chromatin condensation (Fig. S2G, H) but did not display caspase-dependent extrusion or apoptotic body formation (Fig. S2I). These experiments show that the ERK/Akt wave can be triggered by MOMP and correlates with the initial morphological events of apoptosis, independently of caspase activation.

ERK/Akt waves are triggered through paracrine EGFR and MMP signaling.

To explore the signaling networks triggering the spatial ERK/Akt patterns, we treated starved monolayers with different inhibitors, and evaluated the ability of apoptotic cells to trigger signaling waves. Visual inspection of apoptotic nuclear shrinkage was used as a spatial cue to identify ERK/Akt waves. Inhibition of MEK abrogated ERK pulses within apoptosis-triggered signaling waves without having any effect on Akt pulses (Fig.3A, S3A,B, Video S6). Conversely, Akt inhibition abrogated Akt

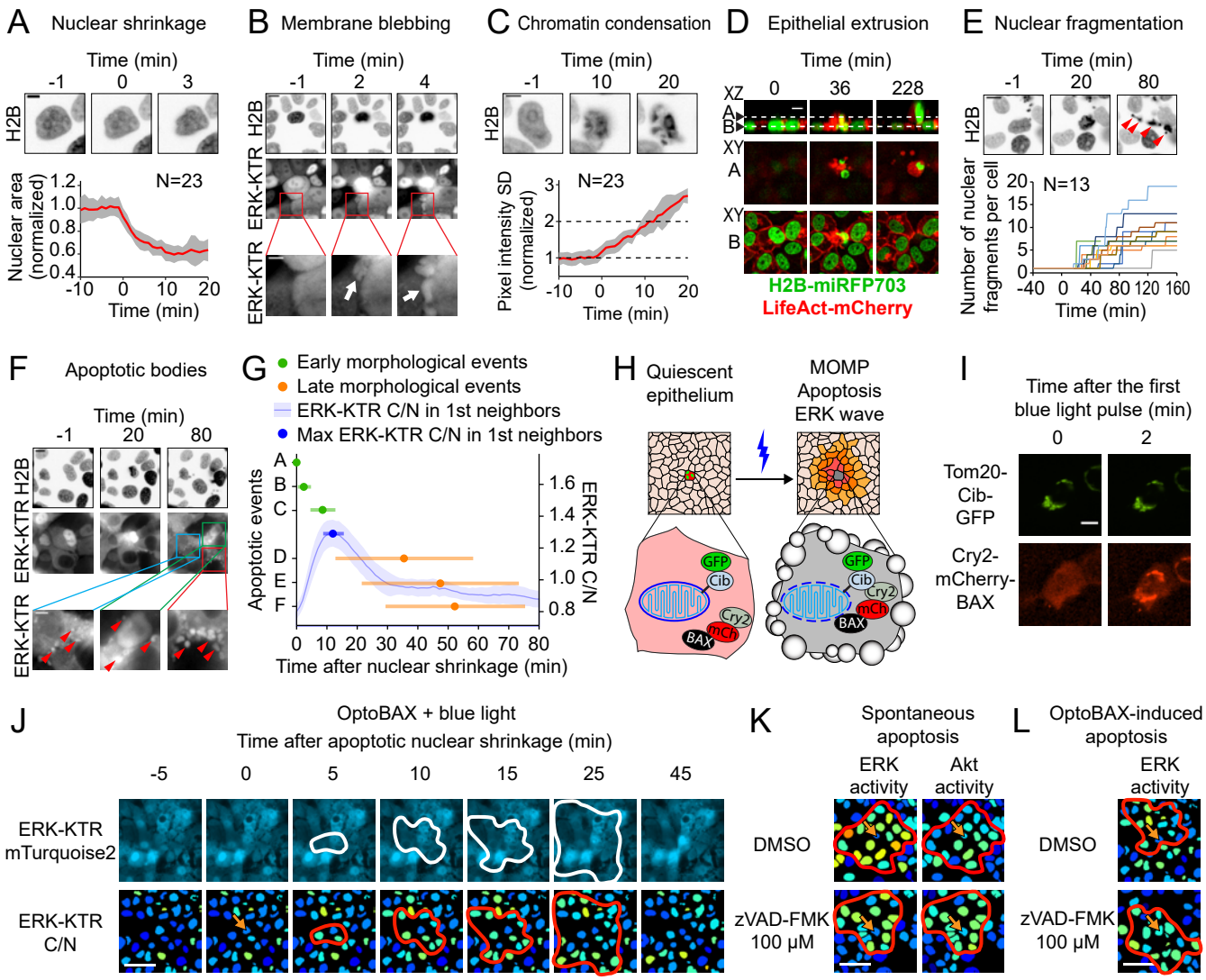

Figure 2: ERK/Akt waves coincide with early morphological events in epithelial apoptosis and can be triggered by optogenetically induced MOMP. (A-F) Examples and quantifications of apoptotic morphological events associated with collective ERK/Akt activity waves. (A) Nuclear shrinkage. The red line and the grey area represent the mean and the standard deviation of the nuclear area, respectively. (B) Membrane blebbing. Blebs are shown in the ERK-KTR channel. (C) Chromatin condensation. Standard deviation of pixel intensity in each nucleus in each time frame has been used as a proxy of nuclear chromatin granularity. The red line and the grey area represent the mean and the standard deviation in multiple apoptotic events. (D) Epithelial extrusion. Optical XZ and XY sections were acquired with a spinning disk confocal microscope with 60x oil-immersion objective. (E) Nuclear fragmentation. Each line represents the number of nuclear fragments for a single apoptotic event. (F) Apoptotic bodies formation. Red arrowheads indicate individual apoptotic bodies in the ERK-KTR channel. **(G)** Temporal distribution of early and late morphological apoptosis events and of max ERK activity in the 1st layer of neighbors. Letters on the left Y-axis correspond to the morphological events shown in panels A-F. Filled circles and horizontal bars represent the mean and the standard deviation, respectively. The blue line depicts the average ERK activity with 95% confidence interval (shade) in the first layer of neighbors. **(H)** Cartoon representing the OptoBAX experiment: MCF10A cells expressing the ERK-KTR biosensor were sparsely transfected with Cry2-mCherry-BAX and the mitochondrial membrane anchor Tom20-Cib-GFP. Upon a whole-field blue light illumination, OptoBAX associates to the mitochondrial membrane causing MOMP dependent apoptosis. **(I)** Snapshots showing the association of OptoBAX to the outer mitochondrial membrane in a cell exposed to blue light. **(J)** ERK activity wave propagating from an OptoBAX-induced apoptotic event. **(K)** ERK/Akt activity wave in the presence of the pan-caspase inhibitor zVAD-FMK. **(L)** ERK activity wave caused by OptoBAX induced apoptosis in presence of zVAD-FMK. Scale bars: (A, C) 5 μm, (B, F) 10 and 5 μm, (D, E, I) 10 μm, (J-L) 50 μm.

waves without any effect on ERK waves (Fig.3A, S3C,D, Video S6). These results suggest that both pathways are independently activated by an upstream signaling node. Paracrine EGFR signaling, which is initiated by the MMPs-mediated cleavage of pro-EGF ligands, has been shown to operate in different epithelial systems (Aoki et al. 2017; Young et al. 2015). Inhibition of EGFR catalytic activity by gefitinib completely abrogated apoptosis-triggered ERK/Akt waves (Fig. 3B, S3E and F, Video S7). Identical results were obtained with the inhibition of ligand binding and receptor dimerization using the anti-EGFR antibody Cetuximab (Fig. 3B, S3G and H, Video S7), as well as with Batimastat-mediated MMP inhibition (Fig. 3B, S3I and J, Video S7). OptoBax-triggered apoptosis yielded identical results (Fig. 3C, S4A-I). These results suggest that ERK/Akt waves depend on MMP-mediated cleavage of pro-EGF ligands (Dong et al. 1999; Aikin et al. 2019) (summarized in Fig. 3D).

ERK/Akt waves do not regulate cell extrusion

Next, we explored the functional significance of the apoptosis-triggered ERK/Akt waves. We first tested the hypothesis that ERK/Akt waves regulate the cytoskeletal process of epithelial extrusion, which requires tight coordination of the apoptotic cell and its neighbors (Gagliardi et al. 2018; Rosenblatt et al. 2001). This hypothesis might be in line with the existence of waves of ERK pulses that regulate myosin contractility to organize collective cell migration (Aoki et al. 2017). Consistently with our observation that ERK/Akt waves temporally overlap with epithelial extrusion (Fig. 2G), we hypothesized that a similar ERK-dependent contractile mechanism might actuate mechanical forces participating in extrusion and/or closing of the epithelial gap. To test this hypothesis, we used a previously established assay (Gagliardi et al. 2018) based on the detection of apoptotic debris extruded in the supernatant to evaluate the cumulative effect of extrusion of an epithelial population (Fig. S5A). Growth factor and serum starvation was used to trigger apoptosis and extrusion in the monolayer. As a control, zVAD-FMK-mediated caspase inhibition, which blocks apoptotic extrusion (Andrade and Rosenblatt 2011), led to low amounts of apoptotic debris in the supernatant (Fig. S5B,C). However, inhibition of ERK/Akt waves using MEK, Akt, EGFR, and MMPs inhibitors did not block this process (Fig. S5D-G). The same result was obtained by direct observation of individual extrusion events (Fig. S5H, Video S8). Altogether, these results suggest that EGFR-dependent ERK/Akt waves do not contribute to cytoskeletal processes during epithelial extrusion.

Apoptosis-triggered ERK/Akt waves provide local survival signals

We then explored whether signaling waves regulate fate decisions. ERK pulses have been implicated in regulation of cell cycle entry in response to EGF (Albeck et al. 2013). However, starved MCF10A cells almost do not proliferate (Ethier and Moorthy 1991). Given that ERK and Akt signaling also regulates survival (Lu and Xu 2006; Franke et al. 2003), we hypothesized that the signaling waves provide local survival signals. To test this hypothesis, we devised computational approaches to explore how spatio-temporally regulated ERK/Akt dynamics might regulate survival and apoptosis fates at the

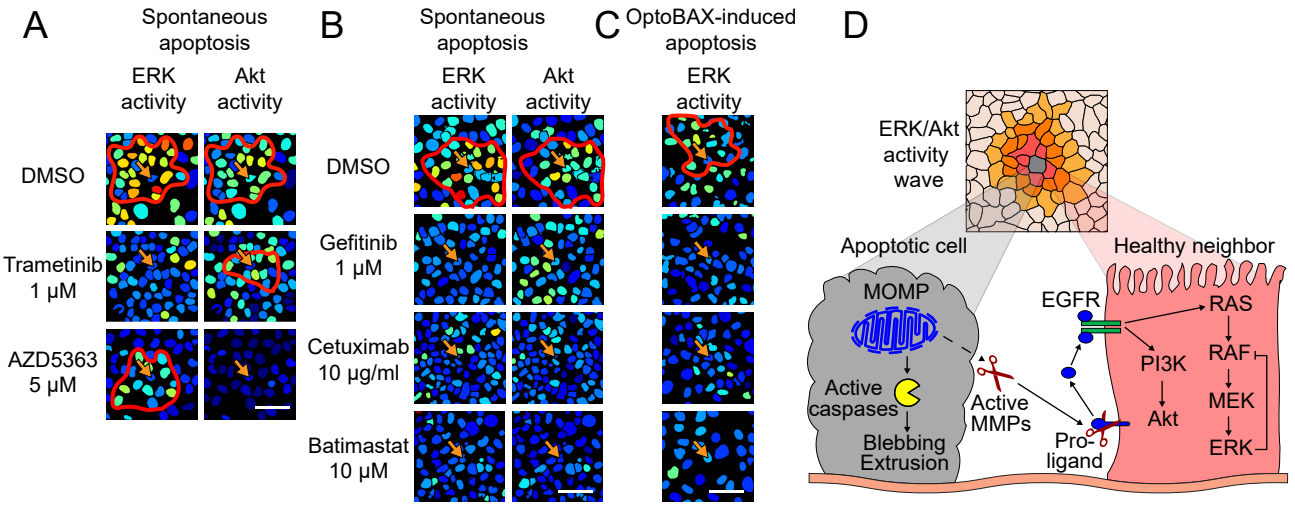

Figure 3: ERK/Akt waves involve EGFR and MMP signaling. (A) ERK or Akt activity waves from apoptotic cells in the presence of Akt inhibitor AZD5363, MEK inhibitor Trametinib or DMSO. Arrows indicate apoptotic cells. **(B)** ERK/Akt activity around apoptotic cells in the presence of EGFR kinase inhibitor Gefitinib, anti-EGFR antibody Cetuximab, pan-MMPs inhibitor Batimastat or DMSO, as a negative control. **(C)** ERK activity after OptoBAX induced apoptosis in the presence of Gefitinib, Cetuximab, Batimastat or DMSO. **(D)** Cartoon of the propagation mechanism of the ERK/Akt activity waves: an apoptotic cell triggers the activation of MMPs that, in turn, cleave a pro-EGFR ligand. The mature form of the ligand then binds and activates EGFR and the downstream signaling network. Scale bar: 50 μm.

single-cell level. We restricted this analysis to ERK signaling because automated identification of collective events required robust signals such as those generated by digital ERK pulses. High quality, 1 minute temporal resolution ERK trajectories were acquired and apoptotic events based on nuclear shrinkage were manually annotated. First, we explored whether ERK activity dynamics differed between apoptotic cells in a 6-hour window before nuclear shrinkage and random non-apoptotic cells during the same period. For that purpose, we trained a convolutional neural network (CNN) with the objective to separate apoptotic from non-apoptotic cells based on ERK activity (Fig. 4A, B, see Methods section for details). A t-distributed stochastic neighbor embedding (tSNE) projection of the data-driven features learnt to separate the classes revealed that apoptotic and non-apoptotic ERK trajectories cluster at each extremity of the tSNE space (Fig. 4A). This indicated that different signaling dynamics are predictive of apoptotic and non-apoptotic fates. Prototype trajectories, for which the model confidence was the highest, suggest that the frequency of ERK pulses is the most discriminative factor used by the CNN to separate apoptotic from non-apoptotic, survival fates (Fig. 4B). Based on this observation, we then ran a peak detection algorithm on the time-series and compared the number of ERK pulses to the fate of cells and to the CNN classification output (Fig. 4C). Trajectories without any ERK pulses corresponded to apoptotic cells in ~65% of the cases. In marked contrast, around 70% of trajectories with 2-5 pulses and 100% with more than 5 pulses corresponded to cells that did not undergo apoptosis. Trajectories with rare, isolated ERK pulses could not be attributed to apoptotic or survival fates (Fig. 4B, C). These results suggest that the apoptosis/survival fates in starved monolayers depend on the ERK pulse frequency.

Second, we evaluated if the different signaling dynamics in apoptotic vs non-apoptotic cells specifically correlated with collective signaling events. To this end, we developed a computational approach that automatically identifies cells involved in collective ERK wave signaling events (Fig. 4D, S6A, Video S9, see Methods section for details). We temporally aligned ERK trajectories of apoptotic cells with respect to apoptotic events, and compared the latter with those of non-apoptotic cells chosen in the same frame and field of view (Fig.4E). We then visualized the occurrence of collective ERK events in these trajectories of apoptotic and non-apoptotic cells. Collective ERK signaling events occurred in only ~32% of apoptotic trajectories, compared to ~53% of randomly-chosen non-apoptotic cells (Fig. 4E, F). Moreover, the collective ERK signaling events were less abundant during a 3-hour window before apoptosis compared to the same time window for randomly chosen non-apoptotic cells (Fig. 4E). These results indicate that cells experiencing collective ERK events are less likely to die than cells that do not.

Third, based on these findings, we explored whether an ERK pulse within an apoptosis-triggered signaling wave locally promotes survival. For that purpose, we evaluated the signaling history of "secondary" apoptotic cells located within the 1st layer of neighbors of a primary apoptotic event (Fig. 4G-I, Video S10). We found that up to 4 hours after the primary apoptosis, secondary apoptosis is significantly less likely to occur in cells that experienced an ERK pulse induced by the primary event (Fig. 4J). This strongly suggests that an ERK activity pulse within an apoptosis-triggered signaling

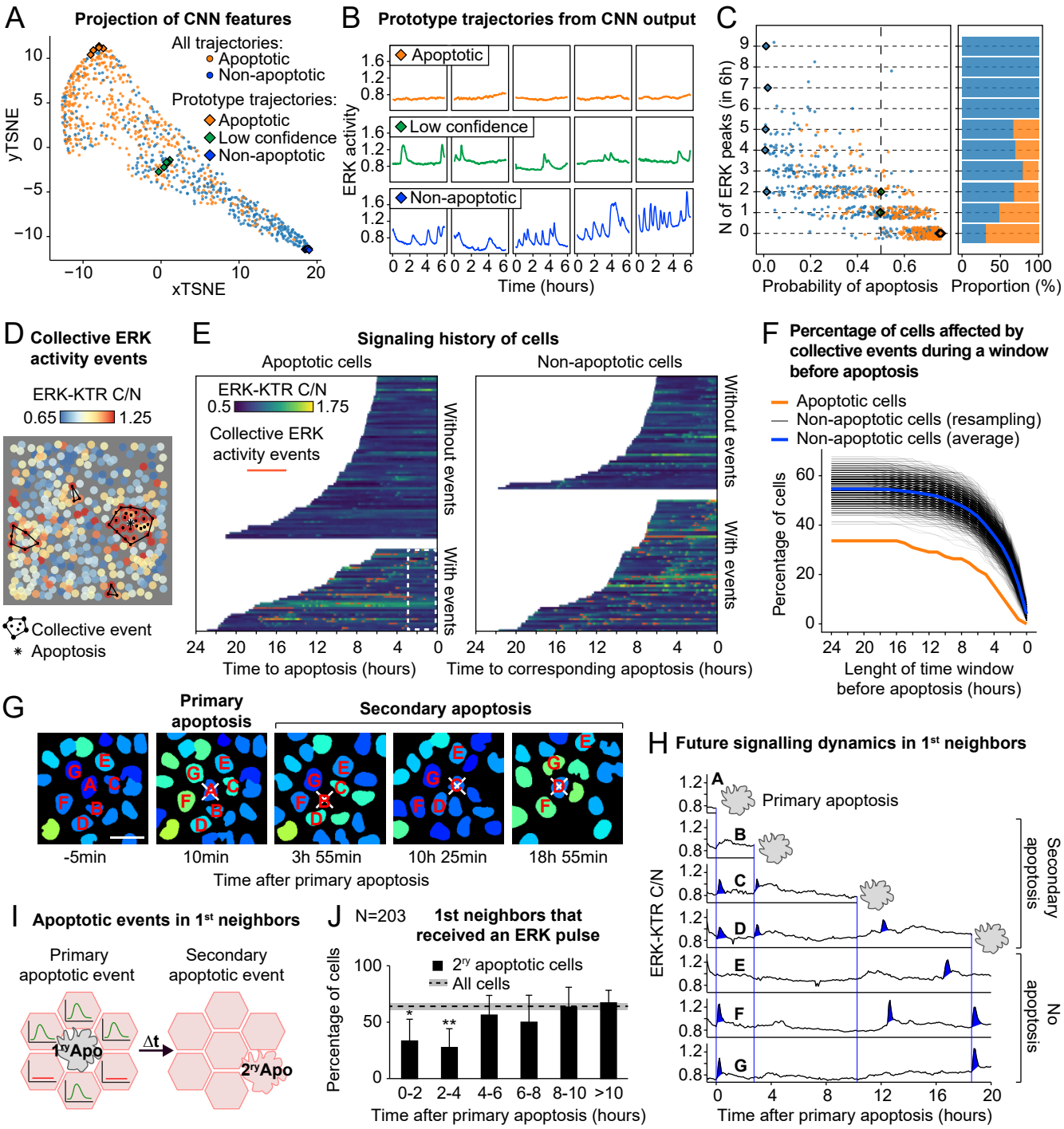

Figure 4: ERK waves drive AiS. (A) tSNE projection of the latent features learnt by the CNN to classify ERK signaling trajectories in apoptotic vs non-apoptotic cells in the 6 hours preceding apoptosis. Each dot represents a single-cell signaling trajectory. Diamonds highlight prototype ERK trajectories of apoptosis (orange), non-apoptosis class (blue) or low-confidence prediction (green). **(B)** Prototype ERK trajectories from A. **(C)** Distribution of ERK trajectories according to the probability of apoptosis predicted by CNN against the number of ERK activity pulses in the trajectories. The right plot shows the proportion of apoptotic vs non-apoptotic cells at each count of ERK activity pulses. **(D)** Automatic identification of collective ERK activity events based on ERK activity. Black polygons indicate collective events; asterisks, apoptotic events. **(E)** Heatmaps of ERK activity in apoptotic vs non-apoptotic cells, randomly chosen in the same frame and field of view as the apoptotic event. The orange overlay indicates times where the cells are involved in collective events. The white dashed box indicates a three-hour window before apoptosis. **(F)** Percentage of cells affected by collective events during a window before apoptosis. The orange line corresponds to apoptotic cells. Black lines represent the result from paired non-apoptotic cells, resampled 1000 times in the same field of view as the corresponding apoptotic cells. Blue line is the average of all resampled curves. **(G)** Example of ERK activity dynamics in consecutive apoptotic events (white crosses) in the first layer of neighbors of a primary apoptotic event indicated "A". Scale bar 20 µm. **(H)** ERK signaling trajectories of consecutive apoptotic events in the first neighborhood from panel G. **(I)** Classification of 1st neighbors of apoptotic cells into those that received or did not receive an ERK activity wave. **(J)** Percentage of secondary apoptotic events in the 1st neighbors that received an ERK activity pulse during 2-hour intervals after the primary apoptotic event. Error bars represent 95% confidence interval. Dashed line and shaded grey area represent the percentage of pulsing cells in all 1st neighbors and 95% confidence interval. Significance with respect to ">10h" calculated with Chi-square test and corrected with the Holm-Bonferroni method (*, $P < 0.05$; **, $P < 0.01$).

wave induces survival for approximately 4 hours. We term the process by which apoptosis-triggered signaling waves locally enforce survival, apoptosis-induced survival (AiS).

Survival fate is modulated by ERK pulsing frequency

Our results suggest that a critical frequency of at least ERK, but potentially also Akt pulses, is required to promote the survival fate in starved monolayers. To establish whether specific dynamic signaling frequencies regulate the survival fate, we used 2 optogenetic systems to evoke synthetic signaling pulse regimes that exhibit different frequencies. We simultaneously measured ERK activity using a spectrally-compatible mRuby2-tagged version of ERK-KTR (Fig. 5A). The first system is a photo-excitable fibroblast growth factor 1-based receptor (OptoFGFR) that activates both ERK and Akt signaling (Kim et al. 2014), and thus mimics the EGFR-dependent signaling observed in our cell system. The second is a photo-excitable RAF construct (OptoRAF) that selectively controls ERK activity only (Aoki et al. 2017). For both systems, a 100 ms of 0.3 W/cm^2 pulse of blue light could induce a robust ERK pulse of similar amplitude (Fig. 5B, C, Video S11). We induced synthetic ERK pulse regimes, with light stimulation applied every 1, 2, 3, 4, 6, 12 hours with both optogenetic systems during a 24-hour period after starvation (Fig. 5D). The ERK pulses were synchronized across the cell population, and their frequency was synchronous with the different stimulation regimes (Fig. 5E,G). Evaluation of the apoptosis rate revealed robust survival when ERK pulses were triggered at least every 3 hours with OptoFGFR (Fig. 5F, Video S12). Protection against apoptosis was intermediate when ERK pulses were triggered every 4 hours, and lost at 6- and 12-hour intervals (Fig. 5F). At the cell population level, this almost completely suppressed the peak of apoptosis triggered by starvation (Fig. S6B). ERK or Akt inhibition abrogated the protection granted by the stimulation of OptoFGFR at high frequency (Fig. S6C). Similar effects were observed with OptoRAF in which high ERK frequencies (1, 2, 3, 4-hour pulse periodicity) provided robust protection that then gradually diminished at lower frequencies (Fig. 5G, H). Using both optogenetic systems, ERK pulses experienced every 3-4 hours are sufficient for protection against apoptosis. Our results using OptoFGFR suggest a role for both ERK and Akt in survival signaling, although we did not evaluate Akt signaling dynamics in this system. The finding that OptoRAF-mediated ERK pulses induce survival at high frequency suggests that ERK signaling is sufficient to exert the pro-survival effects. However, we also found that expression of the OptoRAF system increases survival to some extent (compare basal survival levels, Fig.5F versus 5H), introducing a small bias in our system.

AiS ensures maintenance of tissue integrity in response to stresses of different intensities.

ERK/Akt wave-mediated local survival in the vicinity of apoptotic sites suggests a mechanism that contributes to EH and thus tissue integrity at the level of the cell population in response to stress (such as starvation). To explore that, we evaluated the rate of apoptosis in response to starvation and compared it with population-averaged ERK and Akt activity measurements (Fig.6A). Monolayer starvation

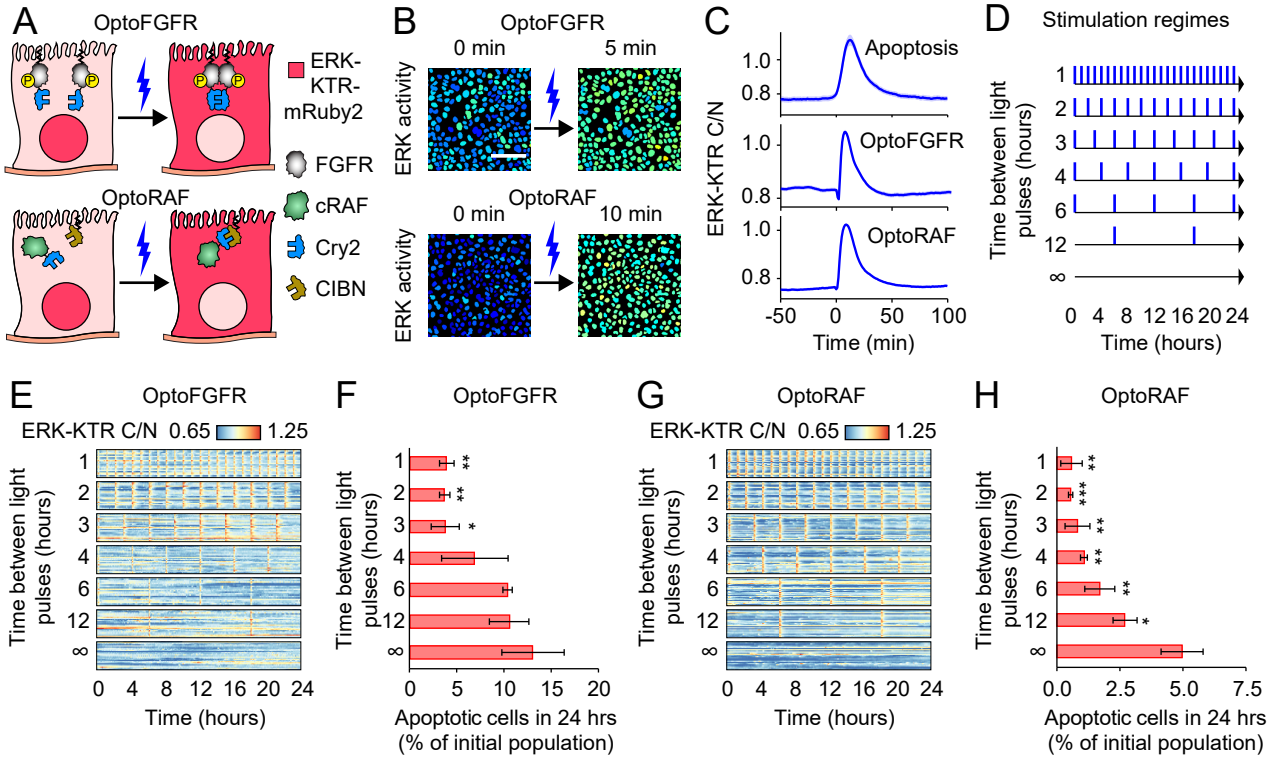

Figure 5: Frequency modulation of ERK pulses regulates the survival fate. (A) Cartoon of the two optogenetic tools used to induce synthetic pulsed ERK signaling regimes. OptoFGFR consists of a CRY2-based, blue-light-dimerizable, plasma-membrane linked FGFR1 intracellular domain. OptoRAF consists of cRAF fused to CRY2 and a plasma membrane-targeted CIBN domain. Blue light can then recruit CRAF to the plasma membrane. **(B)** Examples of ERK activity triggered by OptoFGFR and optoRAF. Representative micrographs show ERK-KTR C/N ratio before and after a blue light pulse. Scale bar 100 µm. **(C)** Average ERK activity trajectories from apoptotic neighbors or from cells expressing OptoFGFR and from cells expressing OptoRAF in response to blue light. The shaded area represents 95% confidence interval. Time of nuclear shrinkage for apoptosis and time of blue light illumination for OptoFGFR and OptoRAF correspond to time 0. **(D)** Different blue light stimulation regimes ranging from 1 pulse/hour to no pulsing. **(E)** ERK signaling trajectories in OptoFGFR expressing cells responding to the stimulation regimes in D. **(F)** Percentage of apoptotic events in OptoFGFR-expressing cells 24 hours after growth factor removal in response to the stimulation regimes in D. **(G,H)** Same as panels E,F but using OptoRAF-expressing cells. Error bars represent the standard deviation of 3 replicate experiments. T test compared to unstimulated cells (*, $P < 0.05$; **, $P < 0.01$; ***, $P < 0.001$).

resulted in a transient peak of apoptosis that started 2-3 hours after starvation, and lasted for another 2-3 hours until a steady-state apoptosis rate ensued. Strikingly, population-averaged ERK/Akt activities immediately decreased with starvation and were transiently re-activated with kinetics that were slightly delayed with respect to the apoptotic rate. This result suggests that the whole monolayer can adapt to starvation-induced stress by dynamically regulating survival to maintain EH and tissue integrity.

To provide intuition about how AiS regulates population-level survival responses, we built a mathematical model to capture the dynamic relationship between apoptosis and survival. The model consists of 2 interacting components: cells undergoing apoptosis, and the protection from cell death that corresponds to the population-averaged ERK/Akt activity triggered by apoptosis (Fig. 6B). The increase in protection level depends on the rate of apoptosis, which in turn is negatively regulated by the amount of protection in the system. The accumulation of protection is modeled as a multistage process, which facilitates a delay in the system. We then varied the rate constants of apoptosis and protection activation, and calculated the fold change in the half-life of the initial cell pool with respect to the half-life of a pure exponential decay, i.e. a model without the protection component (Fig. 6C). We investigated 3 scenarios (Fig. 6C,D). In scenario 1, we set a low rate of apoptosis and a high rate of protection activation to mimic our starvation experiment (Fig. 6D). The model agreed with the starvation experiment (Fig.6A) in that an episode of increased apoptosis is followed by a delayed induction of protection. The increase in the protection level then slows down the apoptosis rate. These alternate periods of protection and apoptosis stem from a positive regulation coupled to a delayed negative regulation and lead to damped oscillations both in the level of protection and in the rate of apoptosis (Fig. 6D).

In scenario 2, we increased the rate of apoptosis that might be induced by a cytotoxic drug. Compared to the first scenario, the model predicted a higher protection level and apoptosis rate after the initial transient (Fig.6D upper panel). Although the cell number decreases faster than in scenario 1, the high protection level prevents cells from dying with the rate of a pure exponential decay (Fig. 6D, lower panel). In scenario 3, we maintained the high apoptosis rate but we lowered the protection rate, which corresponds to a treatment that inhibits the protective effect (e.g. inhibition of ERK/Akt activity). Here, the apoptosis rate exhibits a much slower transient due to a weaker protection (Fig.6D upper panel), leading the cell count to closely follow a pure exponential decay (Fig. 6D, lower panel).

To experimentally validate the results obtained from the mathematical model (scenarios 2/3), we treated our cells with doxorubicin, which induces apoptosis by oxidative stress in MCF10A cells (Gajewski et al. 2007). A dose response screen identified 2.5 and 5 µM doxorubicin as concentrations that induce potent cell death (Fig. S7A). This induced a steep apoptosis increase from 5 to 7 hours after incubation, followed by steady apoptosis levels that corresponded to approximately 3-4% of the cell population per hour for more than 10 hours (Fig. S7B). The steep apoptosis increase was followed by a slightly delayed increase of ERK/Akt population average activity that then remained high (Fig. 6E, S7C and D, Video S13). Lower doxorubicin doses that promoted low apoptosis only led to low ERK/Akt increase (Fig.

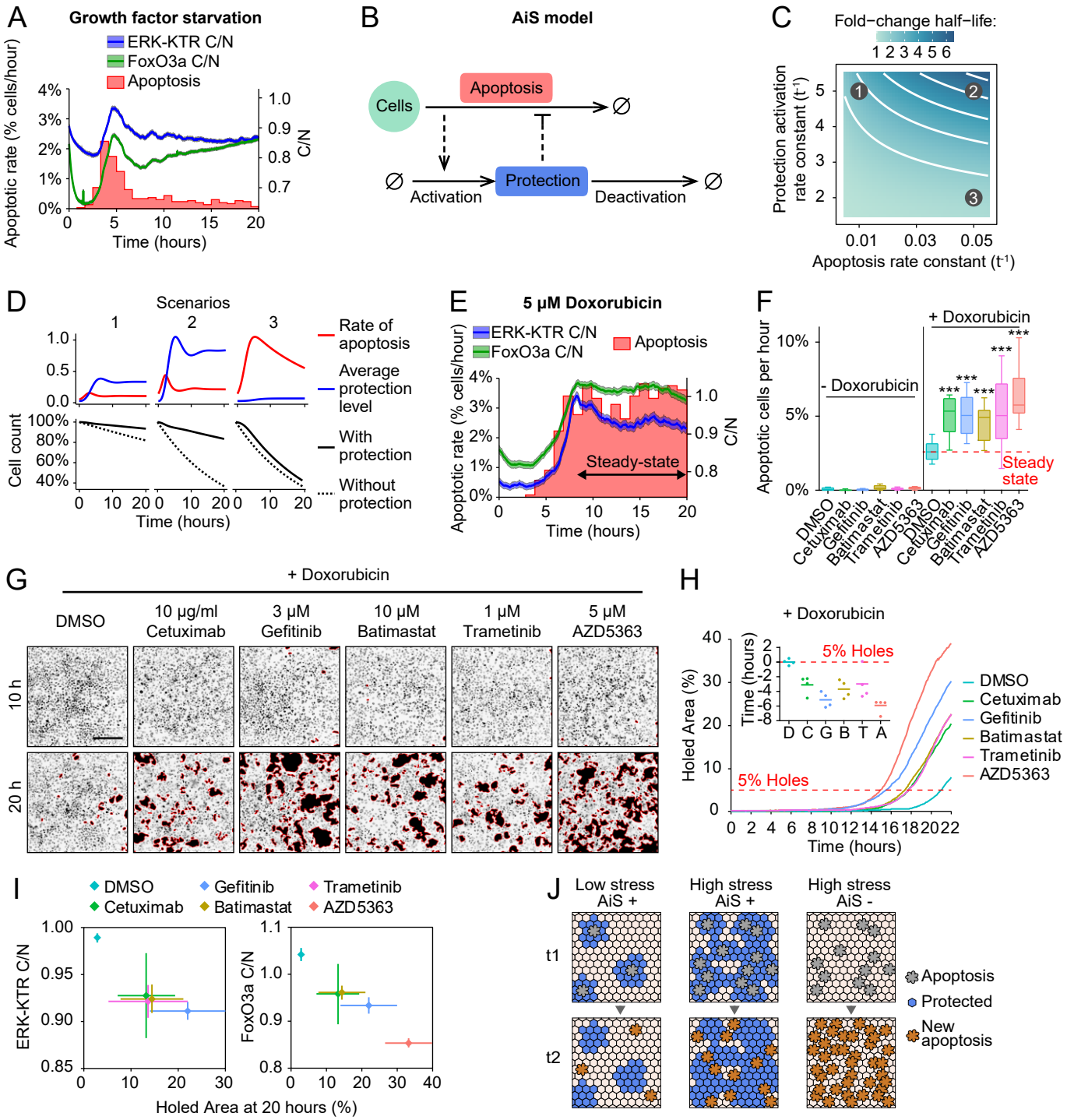

Figure 6: AiS maintains tissue integrity to stresses of different intensities. (A) Rate of apoptotic cells per hour after starvation, superimposed with average ERK/Akt activity trajectories. Shaded areas represent 95% CI. **(B)** Two-component model of AiS. The rate of apoptosis induces the protection, which then inhibits the rate of apoptosis. The onset of protection is multi-stage, which introduces a delay in the apoptosis inhibition. **(C)** Exploration of the model parameter space. Half-decay time of the initial pool of cells calculated as a fold-change with respect to the half-decay time of an exponential decay without induction of protection. Isolines represent 2-6 fold-change half-life. Points indicate 3 scenarios explored in the next panel. **(D)** Predicted rate of apoptosis, protection level and the cell count for 3 scenarios corresponding to: 1 - starved untreated epithelium, 2 - acute pro-apoptotic treatment, 3 - acute pro-apoptotic treatment and AiS inhibition. The cell count is compared to an exponential decay without protection. **(E)** Rate of apoptotic cells per hour after treatment with 5 μM Doxorubicin, superimposed with average ERK and Akt activity trajectories. Shaded areas represent 95% CI. **(F)** Distribution of the rate of apoptotic cells per hour 8-20 hours after Doxorubicin addition and in presence of different treatments. Box plots depict the median and the 25th and 75th percentiles; whiskers correspond to maximum and minimum values. **(G)** Snapshot examples of the nuclear channel from time-lapse experiments of MCF10A epithelium co-treated with doxorubicin and other inhibitors. Holes were detected on ERK-KTR and FoxO3a channels with Ilastik software and represented as black areas with red contours. Scale bar 200 μm. **(H)** Quantification of the percentage of the area occupied by holes from the experiment in G. Each line is the average of 4 different fields of view. 5% of area occupied by holes has been used as a reference time-point to generate the inset chart. Each dot represents a field of view and the horizontal lines the average value. D, DMSO; C, Cetuximab; G, Gefitinib; B, Batimastat; T, Trametinib; A, AZD5363. **(I)** Correlation between ERK or Akt activity and the percentage of the area occupied by holes 20 hours after Doxorubicin addition. Diamonds, average; error bars, standard deviation. **(J)** Cartoon of the population-scale effect of AiS on the epithelium exposed to low or high apoptotic stress in comparison with the same epithelium that lacks AiS. In the presence of AiS, apoptotic events are dispersed and the epithelium can respond to a wide range of stresses.

S7C and D). These results are in line with the predictions of scenario 2 of our model (Fig. 6D). To explore if this sustained population-level ERK/Akt was due to AiS, we inhibited EGFR, MMPs, ERK or Akt and evaluated apoptosis rates. While any of these inhibitors alone had only modest effect on apoptosis, their combination with doxorubicin caused a dramatic increase in the apoptotic rate (Fig. 6F, S8A and B), as predicted in scenario 3 of our model (Fig. 6D). To characterize how changes in apoptosis rate impact on tissue integrity, we measured the speed at which holes were forming in the monolayer. We found that doxorubicin-drug combinations quickly lead to a massive loss of tissue integrity by creating holes in the monolayer that appeared ~15 hours after drug treatment (Fig. 6G and H, Video S14). 20 hours after doxorubicin treatment alone, we observed only small holes that accounted for a maximum of 5% of the monolayer surface. However, after inhibiting the AiS, up to 40% of the surface comprised holes (Fig. 6H). Further, we observed an inverse correlation between population-averaged ERK/Akt activity levels and the holed area 20 hours after doxorubicin treatment (Fig. 6I). These results strongly suggest that single-cell level AiS signaling contributes to population-level tissue integrity by its ability to react to insults of different intensities, and by spatially distancing the apoptotic sites (Fig.6J).

Discussion

Epithelial tissues constantly experience fluctuating stresses and require dynamic coordination of apoptosis, survival and proliferation fates to maintain a critical cell density to preserve barrier function. This involves poorly characterized mechanisms that allow the cell collective to constantly sense the state of the epithelium, and dynamically react by specifying these fate decisions (Macara et al. 2014). We report on AiS, a surprisingly simple multiscale spatial signaling mechanism that preserves EH in response to environmental stresses (Fig. 6J). At the single-cell level, AiS involves apoptosis-triggered, propagating ERK/Akt waves that protect surrounding cells against apoptosis for 3-4 hours. At the population level, this allows the cell collective to dynamically adjust survival fate levels to react to stresses of different intensities, i.e. starvation or cytotoxic challenge. Further, the spatial nature of AiS signaling ensures that cells in close vicinity cannot simultaneously die (Fig.6J), further contributing to tissue integrity even in response to strong stress due to a cytotoxic drug.

Mechanism of wave propagation of ERK/Akt pulses.

An important question is how this ERK/Akt wave is spatially regulated. We find that it depends on canonical EGFR signaling that sequentially triggers radially-propagating ERK/Akt pulses (Fig.3D). The requirement for MMP activity excludes simple diffusion of an EGFR ligand from the apoptotic cell. Rather, cleavage of membrane-bound, precursor EGFR ligands such as EGF or amphiregulin (Dong et al. 1999), might activate signaling in neighboring cells . This might originate a trigger wave, in which each cell layer sequentially activates the next cell layer through EGFR/MMP signaling.

Consistently, similar EGFR/MMP-dependent ERK waves control myosin-dependent contractility to organize collective epithelial cell migration in Madin-Darby Canine Kidney (MDCK) cells (Aoki et al. 2017; Hino et al. 2020). Importantly, MDCK cells also produce apoptosis-triggered ERK waves (Aoki et al. 2013). Together, these results suggest that EGFR/MMP-dependent ERK/Akt waves might be an evolutionary conserved signaling pathway that can function in the regulation of processes such as collective cell migration and AiS-dependent EH.

Another important factor that shapes the signaling wave is the non-linear character of the MAPK cascade (Birtwistle and Kolch 2011). The Raf/MEK/ERK cascade exhibits ultrasensitivity and adaptation (Santos et al. 2007; Ryu et al. 2015; Sparta et al. 2015), which allows to produce short ERK pulses of full amplitude even at low EGFR input. The finding that the number of cells that exhibit digital ERK pulses decreases in the successive layers of the signaling wave (Fig.1I) suggests that the EGFR/MAPK cascade operates at the threshold input required for production of all-or-nothing ERK responses. This is consistent with the minute amounts of EGFR-ligand that might be released by MMP-mediated proteolysis. Thus, the observed reach of the signaling wave that spans up to ~4 layers around the apoptotic event might stem from the architecture of the MAPK network. A similar network logic might produce the Akt transients downstream of EGFR. However, given that the feedbacks in PI3K signaling have been less well characterized, it is difficult to hypothesize about the mechanisms behind Akt pulses.

Fate decision regulation by ERK/Akt pulse frequency

Both EGF stimulation-triggered and apoptosis-triggered ERK/Akt pulses display very similar amplitudes (Fig.1A, B, S1D), and are virtually indistinguishable when compared outside of their spatial context. Our results demonstrate that a very low ERK/Akt pulse frequency correlates with apoptosis, whereas a higher pulse frequency induces survival (Fig.4A-C). In response to EGF stimulation that leads to even higher signaling pulse frequencies than in starved monolayers, cell-cycle entry fate decision directly correlates with EGF concentration-dependent control of ERK pulse frequency (Albeck et al. 2013). This suggests that there are three different ERK/Akt pulse frequency regimes that correlate with apoptosis, survival, and proliferation fates. Indeed, in native tissues where cells constantly experience growth factors and cellular stresses, combinatorial control of ERK/Akt pulses emanating from apoptosis events or growth factors might fine tune EH by equally contributing to survival/proliferation fates.

An immediate question is how a cell interprets the ERK/Akt signaling frequency into these specific fates. Several known ERK or Akt substrates have been implicated in direct actuation of survival, such as the Akt substrate BAD (Datta et al. 1997) or the ERK substrate BIM (Harada et al. 2004). Given that there might be constant phosphatase activity against these ERK/Akt substrates, we envision that the survival effect due to phosphorylation of these direct actuator substrates might be short-lived, allowing the cell collective to constantly reset its survival fate, so as to remain responsive to future apoptotic or

growth factor stimuli. Another fate decision mechanism might indeed involve ERK/Akt-dependent control of transcriptional programs that have evolved to operate at timescales compatible with AiS (Avraham and Yarden 2011). In the case of ERK, this involves immediate early genes (IEGs) that produce highly unstable transcripts with lifetimes of 30-40 minutes, that in turn regulate the transcription of delayed early genes (DEGs) with a lifetime of 1-3 hours. Thus, one digital ERK/Akt pulse might be switching on gene expression that fluctuates on the timescale at which AiS occurs, again allowing the cell collective to reset its survival fate and to remain responsive to future stimuli. Higher signaling frequencies observed in response to EGF stimulation might then allow to control the proliferation fate by regulation of IEGs such as Fra-1 that can linearly integrate ERK activity over time (Gillies et al. 2017). In the future, optogenetic induction of synthetic frequency-modulated signaling regimes might decode how fate decisions are controlled by signaling pulse frequency. Another possible function of Akt pulses might be the single-cell regulation of metabolic activities required for enforcing specific fate decisions (Hung et al. 2017). Finally, we speculate that the ERK pulses that regulate myosin contractility on time scales of minutes to coordinate collective cell migration (Aoki et al. 2017; Hino et al. 2020) might also regulate fate decisions such as survival on timescales of hours. Thus, the MAPK pathway might function in an integrative fashion by regulating processes at different timescales to coordinate both cytoskeletal and survival/proliferation responses during morphogenetic processes.

Population-level AiS responses

Our experiments and computational simulation show that upon the induction of apoptosis, e.g. through starvation or cytotoxic drugs, the feedback embedded in AiS allows the epithelium to dynamically adapt to different apoptotic rates. This might help to mitigate acute spikes of apoptotic rates that potentially compromise epithelial integrity, and to reach a new steady-state rate of apoptosis compatible with the regenerative capability of the epithelial tissue. Given the observation that apoptotic cells produce pro-mitogenic factors (Ryoo et al. 2004; Li et al. 2010), the combined action of AiS and proliferation might maintain EH also under high stress. For example, in our experiments with doxorubicin, we observe approximately 3% of dying cells per hour. Given a 24-hour cell cycle in MCF10A cells, which leads to ~4% population increase per hour, our observed apoptotic rate might be sufficient to maintain a steady-state balance between proliferation and death. Our mechanistic explanation about how inhibition of EGFR-ERK/Akt signaling together with a cytotoxic drug compromises EH and tissue integrity is consistent with numerous reports in which targeted therapies sensitize cancer cells to chemotherapeutic agents (Holt et al. 2012; Smolensky et al. 2017; Barbuti et al. 2019). This provides a rationale to test further targeted/cytotoxic combination therapies to obtain better therapeutic responses for cancers.

Physiological relevance of AiS signaling

Further studies are needed to understand the extent and the significance of AiS *in vivo*. Similar ERK activity waves have also been observed *in vivo* in mouse epithelia (Hiratsuka et al. 2015), suggesting that our cell culture model faithfully recapitulates a physiologically-relevant context. Here the ERK

activity waves correlate with G2/M cell-cycle progression, but it is conceivable that additional inputs not present in our starved monolayer system control this specific fate decision. Recently, Valon and colleagues (Valon et al. 2020) reported apoptosis-triggered, EGFR-dependent ERK pulses during development of the Drosophila pupal notum. This might serve as a mechanism to provide robustness against external perturbations during development. The striking similarities between these different systems suggest that AiS is a highly conserved mechanism regulating epithelial tissue integrity throughout the animal kingdom.

Material and methods

Cell culture and reagents

MCF10A cells were cultured in growth medium composed by DMEM:F12 supplemented with 5% horse serum, 20 ng/ml recombinant human EGF (Peprotech), 10 µg/ml insulin (Sigma-Aldrich/Merck), 0.5 mg/ml hydrocortisone (Sigma-Aldrich/Merck), 200 U/ml penicillin and 200 µg/ml streptomycin. All the experiments were carried out in starvation medium composed by DMEM:F12 supplemented with 0.3% BSA (Sigma-Aldrich/Merck), 0.5 mg/ml hydrocortisone (Sigma-Aldrich/Merck), 200 U/ml penicillin and 200 µg/ml streptomycin. Growth factor and serum starvation experiments were executed by removing the growth medium, 2 washes in PBS and replacement with starvation medium. Transfection of MCF10A cells was carried out with FuGene (Promega) according to the manufacturer protocol. Stable clones with the different biosensors/optogenetic tools were generated by antibiotic selection and image-based screening. AZD5363 (Selleck Chemicals), Batimastat (MedChem Express), Doxorubicin (MedChem Express), Gefitinib (Sigma-Aldrich/Merck), SCH772984 (MedChem Express), Trametinib (Selleck Chemicals) and zVAD-FMK (UBPBio) were dissolved in DMSO and preserved at -20°C in small aliquots to avoid thaw-freeze cycles. Cetuximab was purchased from MedChem Express.

Plasmids

The stable nuclear marker H2B-miRFP703 was generated by fusing the CDS of Homo sapiens H2B clustered histone 11 (H2BC11) with the monomeric near-infrared fluorescent protein miRFP703 CDS (Shcherbakova et al. 2016). ERK-KTR-mTurquoiose2 and ERK-KTR-mRuby2 were generated by fusing the ERK Kinase Translocation Reporter (ERK-KTR) CDS (Regot et al. 2014) with mTurquoiose2 (Goedhart et al. 2012) and mRuby2 (Lam et al. 2012) CDSs, respectively. FoxO3a-mNeonGreen was generated by fusing the 1-1188 portion of the homo sapiens forkhead box O3 a (FoxO3a) CDS with mNeonGreen CDS, a green fluorescent protein derived by Branchiostoma lanceolatum (Shaner et al. 2013). H2B-miRFP703, ERK-KTR-mTurquoiose2, ERK-KTR-mRuby2 and FoxO3a-mNeongreen were cloned in the PiggyBac plasmids pMP-PB, pSB-HPB (gift of David Hacker, Lausanne, (Balasubramanian et al. 2016)), or pPB3.0.Blast, an improved PiggyBac plasmid generated in our lab. For stable DNA integration we transfected the PiggyBac plasmids together with the helper plasmid expressing the transposase (Yusa et al. 2011).

The MOMP optogenetic actuator Cry2(1–531).L348F.mCh.BAX.S184E and Tom20.CIB.GFP, originally designated as the OptoBAX 2.0 system, and here termed as OptoBAX, was generated by Robert M Hughes (Godwin et al. 2019). Lyn-cytoFGFR1-PHR-mCit, expressing myristoylated FGFR1 cytoplasmic region fused with PHR domain of cryptochrome2 and mCitrine, here defined as OptoFGFR, was a gift from Won Do Heo (Addgene plasmid # 59776) (Kim et al. 2014). Lyn-cytoFGFR1-PHR-mCit was subcloned in a lentiviral backbone for stable cell line generation. pPB3.0-

PuroCRY2-cRAF-mCitrine-P2A-CIBN-KrasCT, here defined as OptoRAF, was generated as an improvement of the previously reported light-induced ERK activation system, gift from Kazuhiro Aoki (Aoki et al. 2017). Cloning was done in two steps. First, the CRY2-cRaf sequence was cut from the pCX4puro-CRY2-cRAF plasmid using EcoRI and NotI. mCitrine was PCR amplified from the OptoFGFR plasmid adding NotI and XhoI sites and digested. Both sequences were ligated in the pPB3.0-Puro opened with EcoRI and XhoI. The GSGP2A-CIBN-KRasCT sequence (synthesized by GENWIZ) was digested with BsrGI and AflII and ligated in the opened pPB3.0-Puro-CRY2-cRAF-mCitrine.

Live imaging

MCF10A cells were seeded on 5 µg/ml Fibronectin (PanReac AppliChem) on 24 well 1.5 glass bottom plates (Cellvis) at $1x10^5$ cells/well density two days before the experiment. Imaging experiments were performed on an epifluorescence Eclipse Ti inverted fluorescence microscope (Nikon) controlled by NIS-Elements (Nikon) with a Plan Apo air 20× (NA 0.8) or a Plan Apo air 40× (NA 0.9) objectives. Laser-based autofocus was used throughout the experiments. Image acquisition was performed with an Andor Zyla 4.2 plus camera at a 16-bit depth. The following excitation and emission filters (Chroma) were used: far red: 640nm, ET705/72m; red: 555nm, ET652/60m; NeonGreen: 508nm, ET605/52; GFP: 470nm, ET525/36m; mTurquoise2: 440nm, HQ480/40.

Optogenetic experiments

Cells expressing OptoBAX, OptoFGFR or OptoRAF were kept in the dark for at least 24 hours before the experiments and all preparatory microscope setup was carried out with red or green light (wavelength > 550 nm). In the case of OptoBAX, cells expressing H2B-miRFP703 and ERK-KTR-mTurquoise2 were transfected with OptoBAX plasmids the day before the experiment to obtain sparse transfected cells (< 1% of the total cell population) in the MCF10A epithelium. Cells expressing the OptoBAX system were identified through the expression of Cry2(1–531).L348F.mCh.BAX.S184E fusion protein that contains mCherry. Fields of view containing confluent monolayers and at max 1-2 OptoBAX cells were selected for the experiment. Cells were illuminated with whole field blue light at 440nm every two minutes for the entire duration of the experiment to both induce translocation of BAX to mitochondria and to image ERK-KTR-mTurquoise2. Additionally cells were illuminated at 508nm to visualize Tom20.CIB.GFP, 555nm for mCherry (BAX fusion protein) and 640nm H2B-miRFP703. In the cases of OptoFGFR or OptoRAF, cells expressing H2B-miRFP703 and ERK-KTR-mRuby2 were infected with the lentiviral vector expressing Lyn-cytoFGFR1-PHR-mCit or transfected with pPB3.0.PURO.CRY2.cRAF.mCitrine.P2A.CIBN.KrasCT plasmid to generate stably expressing clones. Cells were imaged at 555nm for mRuby2 and 640nm H2B-miRFP703, and stimulated with 488 nm blue light for 100 ms at 0.3 W/cm^2, when required by the experiment protocol. Stimulation experiments were controlled by NIS jobs.

Image analysis pipeline

For nuclear segmentation, we used a random forest classifier based on different pixel features available in Ilastik software (Berg et al. 2019). For the training phase, we manually annotated nuclear (in 20-50 cells) and background pixels in 16-bit time-lapse TIF images of the nuclear channel (H2B-miRFP703). The probability map of nuclei was then exported as 32-bit TIF images to perform threshold-based segmentation using CellProfiler 3.0 (McQuin et al. 2018). Expansion of nuclear objects by a predefined number of pixels was used to identify the area corresponding to the cytoplasm on a cell-by-cell basis, as described previously (Pargett et al. 2017). Cytosol/nuclear ratio was calculated by dividing the average cytosolic pixel intensity by the average nuclear pixel intensity. For visualization and quality control, we created images of segmented nuclei color coded according to ERK-KTR C/N. Single-cell tracking was performed on nuclear centroids in MATLAB using μ-track 2.2.1 (Jaqaman et al. 2008).
Holes in the epithelial layer were identified by using Ilastik's machine learning approach starting from manual annotation of holes in a combined ERK-KTR-mTurquoiose2 FoxO3a-mNeonGreen channel. After segmentation of hole probability, their total area in each frame and field of view was calculated with Fiji.

Extrusion assay

MCF10A cells were seeded in 6 well plates (TPP Techno Plastic Products AG) at $4x10^5$ cells and grown for 3-4 days till reaching the homeostatic confluent state. The evening before, the wells were washed twice with DMEM:F12, 0.3% BSA, 0.5 mg/ml hydrocortisone, 200 U/ml penicillin and 200 μg/ml streptomycin. After 16h, suspended material, including cell debris, was collected, concentrated and stained for 10 min with Hoechst and CellMask orange (Thermo Fisher). The stained debris were put in between two coverslips and acquired with a widefield fluorescence microscope with a 20x objective. Particles were segmented with CellProfiler 3.0 and data analyzed with R.

Data analysis

To analyze and visualize single-cell ERK/Akt activity time series, we wrote a set of custom R/Python codes. All R notebooks with code required to reproduce the plots and the underlying data are available as supplementary information (link to online repository: http://dx.doi.org/10.17632/kd3n5k784m).

Convolutional Neural Network (CNN)

The convolutional neural network (CNN) was trained as a binary classifier that discriminates between apoptotic and non-apoptotic cells based on their ERK activity time series. These come from four experiments where ERK activity in MCF10A cells was measured every minute. We manually annotated apoptotic cells by visual inspection of the movies and obtained 448 time series with a duration of 8h before the nuclear contraction. To create a balanced dataset and to avoid classification bias towards

either of the classes, we selected 448 random time series of equal duration with cells that did not undergo apoptosis. We performed a data augmentation step by taking random 6h-long segments at every training epoch of the CNN analysis. We chose a plain CNN architecture as described previously (Zhou et al. 2016). It consists of several convolution layers followed by global average pooling (GAP) and a fully connected layer right before the output layer. The advantages of this architecture are a low number of parameters and a strong overfit counterweight with the GAP layer. The architecture comprises 6 successive 1D convolutional layers, all composed of 20 filters except for the last layer with 7 filters. In these layers, the convolution kernel sizes are (5, 5, 5, 5, 3, 3), respectively, with a stride of 1 and a padding that ensures a constant size of the input representation throughout the network. Each convolutional layer is followed by batch normalization and ReLU activation. The whole dataset (training and validation sets) was passed once through the network and the representation of time series after the GAP layer was projected in 2D with tSNE (Fig.4A). Time series that maximized the model confidence for a given class were reported as prototypes. Time series for which entropy of the classification output was maximal (*i.e.* the model returns nearly 50% confidence for both classes) were reported as low-confidence prototypes.

Peak detection

The number of ERK activity peaks (Fig. 4C) was calculated with a custom algorithm that detects local maxima in time series. First, we applied a short median filter to smoothen the data. Then, we ran a long median filter to estimate the long-term bias, which was then subtracted from the smoothed time series. We only kept the positive values. These smoothed and detrended time series were then rescaled to [0,1]. Finally, peaks were detected as points that exceeded a threshold that we manually set at 0.15.

Identification of collective events

To estimate spatial correlations in ERK activity, for every field of view and a time-lapse frame we calculated the local indicators of spatial association (Anselin 1995) using the `lisa` function from the `ncf` package available for R. The function assumes the value of ERK-KTR C/N fluorescence intensity and X/Y positions of the nucleus' centroid. It then outputs the Moran's I autocorrelation coefficient for cells within a radius, which we set to 100px, and the permutation two-sided p-value for each observation based on 1000 resamples. After thresholding cells for the correlation > 0.5 and the p-value < 0.05 we applied the dbscan algorithm from the R package `dbscan` to identify clusters of collective ERK activity. We assumed that a collective event consisted of a minimum 3 cells with the maximum distance between cells of 100px. This procedure yielded individual collective events in each frame of the time lapse movie. We chose only those collective events where ERK-KTR C/N was above a threshold. To estimate the threshold, we performed k-means clustering with 2 centers on individual ERK-KTR C/N values from all collective events. The threshold was the midpoint between the two cluster centers.

Movies of nuclei color-coded according to ERK-KTR C/N with collective events indicated with convex polygons were prepared with `ffmpeg` software from individual png files produced by `ggplot2` in R scripts.

Analysis of cells' history

We matched the X/Y/T coordinates of manually annotated apoptotic events to single-cell time series using the `distance_join` function from the `fuzzyjoin` package for R. Using the maximum euclidean distance of 10px we automatically matched ~95% of apoptotic events. For further analysis, we chose only time series longer than 6h. To plot the ordered heatmaps in Fig. 4E, we overlaid the instances of collective events onto C/N ERK-KTR time series of single cells that underwent apoptosis. As a negative control, for each apoptotic event, we chose a random cell from the same time frame that did not undergo apoptosis during the entire experiment. We only compared sections of time series that matched the lifetime of apoptotic cells. To calculate the average percentage of non-apoptotic cells affected by collective events during a time window before apoptosis of the corresponding apoptotic cell (Fig. 4F), we repeated the selection of random non-apoptotic cells 1000 times.

Mathematical model

The set of ODE equations was solved numerically using the function `ode` from the `deSolve` package in R. The R notebook and an interactive R/Shiny app are available as supplementary material (link to online repository: http://dx.doi.org/10.17632/kd3n5k784m).

$$
\begin{aligned}
C'(t) &= -\frac{k_{apo}}{P_4(t)+1}C(t), \quad C(0)=1 \\
P_1(t) &= k_a(-C'(t)) - k_d P_1(t), \quad P_1(0)=0 \\
P_2(t) &= k_a P_1(t) - k_d P_2(t), \quad P_2(0)=0 \\
P_3(t) &= k_a P_2(t) - k_d P_3(t), \quad P_3(0)=0 \\
P_4(t) &= k_a P_3(t) - k_d P_4(t), \quad P_4(0)=10
\end{aligned}
$$

Where: $C(t)$ - the total number of cells, $P_{1\text{-}4}(t)$ - protection steps, k_{apo} - the rate of apoptosis, k_a - the rate of protection activation, k_d - the rate of protection deactivation. For all simulations k_d was set to 1. Other parameters for scenarios in Fig. 4BC: (1) $k_{apo} = 0.01$, $k_a = 5$, (2) $k_{apo} = 0.05$, $k_a = 5$, (3) $k_{apo} = 0.05$, $k_a = 2$. The ratio $P_3(t)/C(t)$ was used as a measure of the average protection level per cell.

Acknowledgments

This work has been supported by grants from the Swiss National Science Foundation to Olivier Pertz. We thank Won Do Heo for sharing the plasmids coding for OptoFGFR and Kazuhiro Aoki for sharing OptoRAF.

Author contribution

PAG, MD and OP conceived the study. PAG and CD cloned and validated the biosensors. PAG performed experiments and image analysis. MD, M-AJ and PAG analyzed the data. MD performed mathematical modeling. M-AJ performed CNN analyses. CD built the optogenetic toolkit. RMH provided the OptoBAX tool and reviewed the article. OP supervised the work. PAG, MD, M-AJ, CD and OP wrote the paper.

Conflict of interest

The authors declare that they have no conflict of interest

References

Aikin, T.J., Peterson, A.F., Pokrass, M.J., Clark, H.R. and Regot, S. 2019. Collective MAPK signaling dynamics coordinates epithelial homeostasis. *BioRxiv*.

Albeck, J.G., Mills, G.B. and Brugge, J.S. 2013. Frequency-modulated pulses of ERK activity transmit quantitative proliferation signals. *Molecular Cell* 49(2), pp. 249–261.

Andrade, D. and Rosenblatt, J. 2011. Apoptotic regulation of epithelial cellular extrusion. *Apoptosis: An International Journal on Programmed Cell Death* 16(5), pp. 491–501.

Anselin, L. 1995. Local Indicators of Spatial Association-LISA. *Geographical analysis* 27(2), pp. 93–115.

Aoki, K., Kondo, Y., Naoki, H., Hiratsuka, T., Itoh, R.E. and Matsuda, M. 2017. Propagating wave of ERK activation orients collective cell migration. *Developmental Cell* 43(3), pp. 305-317.e5.

Aoki, K., Kumagai, Y., Sakurai, A., et al. 2013. Stochastic ERK activation induced by noise and cell-to-cell propagation regulates cell density-dependent proliferation. *Molecular Cell* 52(4), pp. 529–540.

Avraham, R. and Yarden, Y. 2011. Feedback regulation of EGFR signalling: decision making by early and delayed loops. *Nature Reviews. Molecular Cell Biology* 12(2), pp. 104–117.

Balasubramanian, S., Wurm, F.M. and Hacker, D.L. 2016. Multigene expression in stable CHO cell pools generated with the piggyBac transposon system. *Biotechnology Progress* 32(5), pp. 1308–1317.

Barbuti, A.M., Zhang, G.-N., Gupta, P., Narayanan, S. and Chen, Z.-S. 2019. EGFR and HER2 inhibitors as sensitizing agents for cancer chemotherapy. In: *Protein kinase inhibitors as sensitizing agents for chemotherapy*. Elsevier, pp. 1–11.

Berg, S., Kutra, D., Kroeger, T., et al. 2019. ilastik: interactive machine learning for (bio)image analysis. *Nature Methods* 16(12), pp. 1226–1232.

Bezler, M., Hengstler, J.G. and Ullrich, A. 2012. Inhibition of doxorubicin-induced HER3-PI3K-AKT signalling enhances apoptosis of ovarian cancer cells. *Molecular Oncology* 6(5), pp. 516–529.

Bilak, A., Uyetake, L. and Su, T.T. 2014. Dying cells protect survivors from radiation-induced cell death in Drosophila. *PLoS Genetics* 10(3), p. e1004220.

Birtwistle, M.R. and Kolch, W. 2011. Biology using engineering tools: the negative feedback amplifier. *Cell Cycle* 10(13), pp. 2069–2076.

Darwich, A.S., Aslam, U., Ashcroft, D.M. and Rostami-Hodjegan, A. 2014. Meta-analysis of the turnover of intestinal epithelia in preclinical animal species and humans. *Drug Metabolism and Disposition: the Biological Fate of Chemicals* 42(12), pp. 2016–2022.

Datta, S.R., Dudek, H., Tao, X., et al. 1997. Akt phosphorylation of BAD couples survival signals to the cell-intrinsic death machinery. *Cell* 91(2), pp. 231–241.

Dong, J., Opresko, L.K., Dempsey, P.J., Lauffenburger, D.A., Coffey, R.J. and Wiley, H.S. 1999. Metalloprotease-mediated ligand release regulates autocrine signaling through the epidermal growth factor receptor. *Proceedings of the National*

Academy of Sciences of the United States of America 96(11), pp. 6235–6240.
Eisenhoffer, G.T., Loftus, P.D., Yoshigi, M., et al. 2012. Crowding induces live cell extrusion to maintain homeostatic cell numbers in epithelia. *Nature* 484(7395), pp. 546–549.
Ethier, S.P. and Moorthy, R. 1991. Multiple growth factor independence in rat mammary carcinoma cells. *Breast Cancer Research and Treatment* 18(2), pp. 73–81.
Franke, T.F., Hornik, C.P., Segev, L., Shostak, G.A. and Sugimoto, C. 2003. PI3K/Akt and apoptosis: size matters. *Oncogene* 22(56), pp. 8983–8998.
Gagliardi, P.A., Somale, D., Puliafito, A., et al. 2018. MRCKα is activated by caspase cleavage to assemble an apical actin ring for epithelial cell extrusion. *The Journal of Cell Biology* 217(1), pp. 231–249.
Gajewski, E., Gaur, S., Akman, S.A., Matsumoto, L., van Balgooy, J.N.A. and Doroshow, J.H. 2007. Oxidative DNA base damage in MCF-10A breast epithelial cells at clinically achievable concentrations of doxorubicin. *Biochemical Pharmacology* 73(12), pp. 1947–1956.
Gillies, T.E., Pargett, M., Minguet, M., Davies, A.E. and Albeck, J.G. 2017. Linear Integration of ERK Activity Predominates over Persistence Detection in Fra-1 Regulation. *Cell Systems* 5(6), pp. 549-563.e5.
Godwin, W.C., Hoffmann, G.F., Gray, T.J. and Hughes, R.M. 2019. Imaging of morphological and biochemical hallmarks of apoptosis with optimized optogenetic tools. *The Journal of Biological Chemistry* 294(45), pp. 16918–16929.
Goedhart, J., von Stetten, D., Noirclerc-Savoye, M., et al. 2012. Structure-guided evolution of cyan fluorescent proteins towards a quantum yield of 93%. *Nature Communications* 3, p. 751.
Gudipaty, S.A., Lindblom, J., Loftus, P.D., et al. 2017. Mechanical stretch triggers rapid epithelial cell division through Piezo1. *Nature* 543(7643), pp. 118–121.
Gu, Y., Forostyan, T., Sabbadini, R. and Rosenblatt, J. 2011. Epithelial cell extrusion requires the sphingosine-1-phosphate receptor 2 pathway. *The Journal of Cell Biology* 193(4), pp. 667–676.
Harada, H., Quearry, B., Ruiz-Vela, A. and Korsmeyer, S.J. 2004. Survival factor-induced extracellular signal-regulated kinase phosphorylates BIM, inhibiting its association with BAX and proapoptotic activity. *Proceedings of the National Academy of Sciences of the United States of America* 101(43), pp. 15313–15317.
Hino, N., Rossetti, L., Marín-Llauradó, A., et al. 2020. ERK-Mediated Mechanochemical Waves Direct Collective Cell Polarization. *Developmental cell*.
Hiratsuka, T., Fujita, Y., Naoki, H., Aoki, K., Kamioka, Y. and Matsuda, M. 2015. Intercellular propagation of extracellular signal-regulated kinase activation revealed by in vivo imaging of mouse skin. *eLife* 4, p. e05178.
Holt, S.V., Logié, A., Odedra, R., et al. 2012. The MEK1/2 inhibitor, selumetinib (AZD6244; ARRY-142886), enhances anti-tumour efficacy when combined with conventional chemotherapeutic agents in human tumour xenograft models. *British Journal of Cancer* 106(5), pp. 858–866.
Hung, Y.P., Teragawa, C., Kosaisawe, N., et al. 2017. Akt regulation of glycolysis mediates bioenergetic stability in epithelial cells. *eLife* 6.
Jaqaman, K., Loerke, D., Mettlen, M., et al. 2008. Robust single-particle tracking in live-cell time-lapse sequences. *Nature Methods* 5(8), pp. 695–702.
Kim, N., Kim, J.M., Lee, M., Kim, C.Y., Chang, K.-Y. and Heo, W.D. 2014. Spatiotemporal control of fibroblast growth factor receptor signals by blue light. *Chemistry & Biology* 21(7), pp. 903–912.
Lam, A.J., St-Pierre, F., Gong, Y., et al. 2012. Improving FRET dynamic range with bright green and red fluorescent proteins. *Nature Methods* 9(10), pp. 1005–1012.
Li, F., Huang, Q., Chen, J., et al. 2010. Apoptotic cells activate the “phoenix rising” pathway to promote wound healing and tissue regeneration. *Science Signaling* 3(110), p. ra13.
Lu, Z. and Xu, S. 2006. ERK1/2 MAP kinases in cell survival and apoptosis. *IUBMB Life* 58(11), pp. 621–631.
Macara, I.G., Guyer, R., Richardson, G., Huo, Y. and Ahmed, S.M. 2014. Epithelial homeostasis. *Current Biology* 24(17), pp. R815-25.

Marinari, E., Mehonic, A., Curran, S., Gale, J., Duke, T. and Baum, B. 2012. Live-cell delamination counterbalances epithelial growth to limit tissue overcrowding. *Nature* 484(7395), pp. 542–545.

McQuin, C., Goodman, A., Chernyshev, V., et al. 2018. CellProfiler 3.0: Next-generation image processing for biology. *PLoS Biology* 16(7), p. e2005970.

Pargett, M., Gillies, T.E., Teragawa, C.K., Sparta, B. and Albeck, J.G. 2017. Single-Cell Imaging of ERK Signaling Using Fluorescent Biosensors. *Methods in Molecular Biology* 1636, pp. 35–59.

Pérez-Garijo, A., Fuchs, Y. and Steller, H. 2013. Apoptotic cells can induce non-autonomous apoptosis through the TNF pathway. *eLife* 2, p. e01004.

Regot, S., Hughey, J.J., Bajar, B.T., Carrasco, S. and Covert, M.W. 2014. High-sensitivity measurements of multiple kinase activities in live single cells. *Cell* 157(7), pp. 1724–1734.

Rosenblatt, J., Raff, M.C. and Cramer, L.P. 2001. An epithelial cell destined for apoptosis signals its neighbors to extrude it by an actin- and myosin-dependent mechanism. *Current Biology* 11(23), pp. 1847–1857.

Ryoo, H.D., Gorenc, T. and Steller, H. 2004. Apoptotic cells can induce compensatory cell proliferation through the JNK and the Wingless signaling pathways. *Developmental Cell* 7(4), pp. 491–501.

Ryu, H., Chung, M., Dobrzyński, M., et al. 2016. Frequency modulation of ERK activation dynamics rewires cell fate. *Molecular Systems Biology* 12(4), p. 866.

Ryu, H., Chung, M., Dobrzyński, M., et al. 2015. Frequency modulation of ERK activation dynamics rewires cell fate. *Molecular Systems Biology* 11(11), p. 838.

Sampattavanich, S., Steiert, B., Kramer, B.A., Gyori, B.M., Albeck, J.G. and Sorger, P.K. 2018. Encoding Growth Factor Identity in the Temporal Dynamics of FOXO3 under the Combinatorial Control of ERK and AKT Kinases. *Cell Systems* 6(6), pp. 664-678.e9.

Santos, S.D.M., Verveer, P.J. and Bastiaens, P.I.H. 2007. Growth factor-induced MAPK network topology shapes Erk response determining PC-12 cell fate. *Nature Cell Biology* 9(3), pp. 324–330.

Saraste, A. and Pulkki, K. 2000. Morphologic and biochemical hallmarks of apoptosis. *Cardiovascular Research* 45(3), pp. 528–537.

Shaner, N.C., Lambert, G.G., Chammas, A., et al. 2013. A bright monomeric green fluorescent protein derived from Branchiostoma lanceolatum. *Nature Methods* 10(5), pp. 407–409.

Shcherbakova, D.M., Baloban, M., Emelyanov, A.V., Brenowitz, M., Guo, P. and Verkhusha, V.V. 2016. Bright monomeric near-infrared fluorescent proteins as tags and biosensors for multiscale imaging. *Nature Communications* 7, p. 12405.

Smolensky, D., Rathore, K., Bourn, J. and Cekanova, M. 2017. Inhibition of the PI3K/AKT Pathway Sensitizes Oral Squamous Cell Carcinoma Cells to Anthracycline-Based Chemotherapy In Vitro. *Journal of Cellular Biochemistry* 118(9), pp. 2615–2624.

Sparta, B., Pargett, M., Minguet, M., Distor, K., Bell, G. and Albeck, J.G. 2015. Receptor Level Mechanisms Are Required for Epidermal Growth Factor (EGF)-stimulated Extracellular Signal-regulated Kinase (ERK) Activity Pulses. *The Journal of Biological Chemistry* 290(41), pp. 24784–24792.

Valon, L., Levillayer, F., Davidovič, A., Chouly, M., Cerqueira-Campos, F. and Levayer, R. 2020. Robustness of epithelial sealing is an emerging property of local ERK feedbacks driven by cell elimination. *BioRxiv*.

Young, C.D., Zimmerman, L.J., Hoshino, D., et al. 2015. Activating PIK3CA Mutations Induce an Epidermal Growth Factor Receptor (EGFR)/Extracellular Signal-regulated Kinase (ERK) Paracrine Signaling Axis in Basal-like Breast Cancer. *Molecular & Cellular Proteomics* 14(7), pp. 1959–1976.

Yusa, K., Zhou, L., Li, M.A., Bradley, A. and Craig, N.L. 2011. A hyperactive piggyBac transposase for mammalian applications. *Proceedings of the National Academy of Sciences of the United States of America* 108(4), pp. 1531–1536.

Zhou, B., Khosla, A., Lapedriza, A., Oliva, A. and Torralba, A. 2016. Learning deep features for discriminative localization. In: *Proceedings of 2016 IEEE Conference on Computer Vision and Pattern Recognition (CVPR)*. IEEE, pp. 2921–2929.